Effect of Sr Addition to a Modified AA3003 on Microstructural and Corrosion Properties

Verkens, Donovan; Revilla, Reynier I.; Huizenga, Richard; Marcoen, Kristof; Günyüz, Mert; Işiksaçan, Cemil; Terryn, Herman; De Graeve, Iris

DOI
10.1149/1945-7111/abdfaa

Publication date
2021

Document Version
Final published version

Published in
Journal of the Electrochemical Society

Journal of The Electrochemical Society

The Electrochemical Society
Advancing solid state & electrochemical science & technology

Effect of Sr Addition to a Modified AA3003 on Microstructural and Corrosion Properties

Journal of The Electrochemical Society, 2021 **168** 021506

Effect of Sr Addition to a Modified AA3003 on Microstructural and Corrosion Properties

Donovan Verkens,[1,z] Reynier I. Revilla,[1] Richard Huizenga,[2] Kristof Marcoen,[1] Mert Günyüz,[3] Cemil Işıksaçan,[3] Herman Terryn,[1,*] and Iris De Graeve[1]

[1]*Electrochemical and Surface Engineering (SURF), Vrije Universiteit Brussel (VUB), Brussels, Belgium*
[2]*Department of Materials Science and Engineering, Delft University of Technology, Delft, The Netherlands*
[3]*R&D, Assan Alüminyum A.Ş., Istanbul, Turkey*

Sr is known to transform the morphology of the eutectic silicon phase as well as the Fe-rich β phase in Al-Si alloys, improving their mechanical properties. However, little is known about the effect Sr has on the (local) corrosion properties of aluminium alloys. This study investigates the effect of Sr addition to a modified AA3003 heat exchanger material on the morphology of the different phases present, especially the Fe-rich phases, as well as on the (local) corrosion properties of this material. This work reports the formation of a Sr-rich phase, which slightly increases the macrohardness of the material. The Fe-rich phases are not shown to be refined/influenced by the addition of Sr Potentiodynamic polarization experiments showed an increase in pitting potential by increasing the amount of Sr in the material up to 0.4 wt.%. Nevertheless, the analysis of the corrosion morphology revealed that the Sr-containing particles did not contribute to the corrosion process despite their cathodic behaviour compared to the Al matrix as measured by Scanning Kelvin Probe Force Microscopy. This behaviour was attributed to the thicker oxide layer found on the Sr-rich particles.

 [DOI: 10.1149/1945-7111/abdfaa]

Manuscript submitted December 18, 2020; revised manuscript received January 21, 2021. Published February 3, 2021. *This paper is part of the JES Focus Issue on Characterization of Corrosion Processes in Honor of Philippe Marcus.*

Strontium is well known to act as a modifier in Al-Si cast alloys. When a small amount of strontium is added to Al-Si cast alloys, it transforms the morphology of the eutectic silicon phase from coarse plate-like to a fine fibrous network. This results in more favourable mechanical properties of Al-Si cast alloys.[1,2] However, the effect of the addition of Sr on the corrosion properties of Al-Si alloys is not well understood. Some research shows worsened corrosion behaviour, attributed to the increased area at the interface between the matrix and the silicon phase.[3,4] While other research shows an improvement of the corrosion resistance with Sr addition, due to the formation of a more compact and less defective oxide layer.[5] Furthermore, Al-Si cast alloys often contain impurities and trace elements, like Fe, Mn, Cr. These elements will form hard and high melting point intermetallics, like for instance the $\beta - Al_5FeSi$ phase. However, this AlFeSi phase is detrimental for the mechanical properties of Al-Si cast alloys. Additionally, the addition of Sr to Al-Si alloys results in the modification of the large and highly branched needle-like AlFeSi phase to one that is less branched, smaller and has a lower volume fraction.[6] This change in morphology of the intermetallic phases may have an effect on the corrosion properties of the alloy. Given the cathodic behaviour of the intermetallics, a change in their morphology could imply a change in their cathodic behaviour. Besides improving the mechanical properties of Al-Si alloys, Sr is also shown to decrease sensitization in Al-Mg-Mn alloys. The increased intergranular corrosion resistance is attributed to a decrease in the $\beta - Mg_2Al_3$ phase at the grain boundaries, making the grain boundaries less anodic in nature.[7,8]

In the present work Sr was added to the AA 3003 alloy for improved mechanical properties. However, the impact of its addition on the corrosion resistance is unknown and this is of course a critical issue. In these heat exchangers, the tube and fin material are brazed together by means of an AA4xxx alloy, which has a eutectic temperature lower than the melting temperature of the fin and tube material.[9] The corrosion properties of a Direct Chill (DC) casted AA3003 are well known and there are some studies available in literature.[10,11] A high pitting factor was reported after a statistical evaluation of the susceptibility to pitting corrosion of DC casted AA3003 by Paredes-Dugarte et al., indicating a highly localised corrosion process in a saline environment.[10] An integrated atomic force microscopy and scanning electrochemical microscopy (AFM/SECM) approach was used by Davoodi et al. to investigate the localised activity at the surface of DC-casted AA3003 in a saline solution.[11] The combination of these two techniques reported the cathodic activity of the intermetallic particles. The in situ AFM measurements, performed in an acetic acid solution at OCP, showed the localised dissolution of the aluminium matrix adjacent to the intermetallic particles as well. Furthermore, the formation of deposits of ring-like corrosion products was reported. Moreover, Davoodi et al. reported that the larger intermetallic particles in the AA3003 cause more localised corrosion than the submicrometric dispersoids.[11] The AA3003 contains the following primary eutectic phases before homogenisation: the Al(Mn,Fe) phase, typically $Al_6(Mn, Fe)$, and the α-Al(Mn,Fe)Si phase, typically $\alpha - Al_{15}(Mn, Fe)_3Si_2$.[11–13] However, a certain amount of the $\beta - Al_5FeSi$ phase could still possibly remain. To the best of our knowledge no work has been done on the effect of the addition of Sr to Al-Mn alloys, like for instance AA3003. This is however of great importance given the fact that it was already shown that Sr modifies the morphology of the Fe-rich $\beta - Al_5FeSi$ phase in Al-Si alloys. Therefore, Sr could potentially modify the morphology of the Fe-rich phases in Al-Mn alloys, like the $\beta - Al_5FeSi$ phase present in Al-Mn alloys as well. Additionally, the potential change in morphology could have an effect on the corrosion properties, that when used in applications like for instance heat exchangers determine their life time. Moreover, given the fact that Sr is used in several aluminium alloy systems,[1–8] studying the effect of Sr addition to Fe-containing Al-Mn alloys is key in understanding the corrosion and local corrosion behaviour of Sr in aluminium alloys. Therefore, this work focuses on studying the effect of the addition of Sr to a modified AA3003 on the microstructure (morphology of the primary phases) and corrosion properties. First the microstructure was investigated by using a thermodynamic simulation software to predict the stable, most likely phases present. Then this model microstructure was evaluated by investigating the real microstructure by scanning electron microscopy/energy dispersive X-ray

*Electrochemical Society Member.
[z]E-mail: donovan.verkens@vub.be

spectroscopy (SEM/EDS), optical microscopy and Time-of-flight secondary ion mass spectrometry (ToF-SIMS). The corrosion properties were determined by a set of potentiodynamic polarization experiments and immersion tests. And finally, Scanning Kelvin Probe Force Microscopy (SKPFM) was used to evaluate the interaction between the different phases.

Experimental

Samples.—The Al-Mn alloys were cast by Assan Aluminyum in a steel mold by liquid metal casting. Three different alloys were casted: the modified AA3003 and the two Sr-containing alloys. All the samples were mechanically ground and polished, finishing with 0.04 μm standard colloidal silica suspension (OP-S). The chemical compositions of the alloys were provided by Assan Alüminyum and are shown in Table I.

Electrochemical measurements.—All the electrochemical measurements were carried out in a three-electrode cell configuration using an AUTOLAB Potentiostat-Galvanostat (PGSTAT 30) with the sample as the working electrode, a platinum counter electrode, and a saturated Ag/AgCl reference electrode. A 0.1 M NaCl solution was used as an electrolyte at room temperature. The open circuit potential (OCP) was monitored for 1 h at a measuring interval of 0.1 s, so that the system could stabilize before the potentiodynamic polarization measurements. Two types of potentiodynamic polarization tests were performed at a rate of 0.1 V min^{-1}: the first starting at 20 mV below OCP towards the positive direction to 0.8 V above OCP and the second starting at 20 mV above OCP in the negative direction to −1.3 V with respect to the reference electrode potential. Different samples were used for these anodic and cathodic polarizations, respectively. An automatic current range was selected between 10 nA and 1 A. The potentiodynamic polarization measurements were performed three to five times for each alloy. From these measurements, the pitting potential was determined for each alloy.

Surface characterisation.—The characterisation of the microstructure, the corrosion morphology, and the native oxide layer was done using optical microscopy (with a Leica DMi8 microscope), SEM/EDS, ToF-SIMS, X–ray photoelectron spectroscopy (XPS), and Auger electron spectroscopy (AES). For the SEM/EDS analysis, a JOEL JSM-IT300 was used with an acceleration voltage of 30 kV, a working distance of 10 mm and a probe current of 1 nA.

ToF-SIMS measurements were performed with a TOF-SIMS 5 system from IONTOF GmbH (Münster, Germany), using a 30 keV Bi_3^+ primary ion beam operated in the high current bunched mode for high mass resolution (approximately 8000 at 29 m z^{-1} (^{29}Si$^+$)). The lateral resolution achieved in high current bunched mode is 3 μm. The pulsed ion beam target current was 0.70 pA. Positive ion mass spectra were acquired over a mass range of 1–800 m z^{-1}. The total ion dose was kept below the static limit of 10^{13} ions cm^{-2} analysis^{-1}. A large area image was obtained on the Sr-containing alloy with 0.4 wt% Sr of 500 μm × 500 μm. XPS spectra were collected using a VersaProbe II photoelectron spectroscope (Physical Electronics) with an Al Kα monochromatic X-ray source (1486.6 eV of photons). The vacuum in the analysis chamber was approximately 5´10^{-7} Pa during measurements. High-resolution scans of the Al2p and O1s photoelectron peaks were recorded from a spot diameter of 100 μm using a pass energy of 26.5 eV and a step size of 0.1 eV. Measurements were performed with a takeoff angle of 45° with respect to the sample surface. The AES was performed by a JEOL JAMP-9500F. A 10 kV electron beam operating at 1 nA was used. The sample holder was tilted 30° relative to the electron beam and positioned at a working distance of 23 mm. The set-up was equipped with a hemispherical analyzer with seven channeltrons, positioned at 60° to the electron gun. The depth profiles were made by 19 cycles of spectra acquisition and sputtering, in locations on top of: Fe-rich particles, Sr-containing particles, and the matrix. A 30-second sputtering cycle using the Ar$^+$ float gun at 500 eV acceleration voltage and an Ar gas pressure of

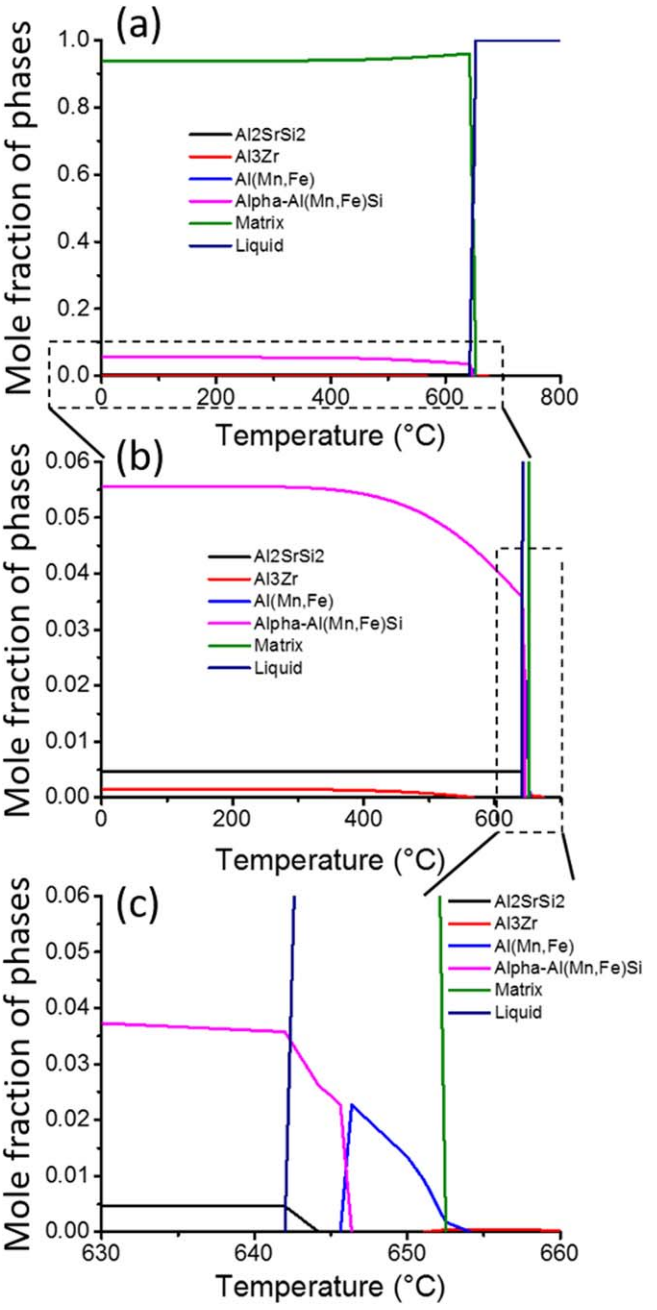

Figure 1. Thermo-calc calculation of the equilibrium solidification of the base alloy with addition of Sr, (b) a magnified view of (a), and (c) a magnified view of (b).

Table I. Chemical composition of the different lab casted alloys, with x = 0, 0.2, and 0.4 (wt%).

Si	Fe	Mn	Mg	Zn	Cu	Zr	Sr	Al
0.70–0.80	0.40–0.50	1.40–1.60	0–0.02	1.40–1.60	0.05–0.10	0.05–0.20	×	Balance

7.5 10^{-2} Pa was used. The resulting etching rate was around 1.8 nm min^{-1} as calibrated on SiO2. The thermodynamic software Thermo-Calc was used to predict the possible phases that could form during equilibrium solidification of the Sr-containing alloys. Additionally, in order to simulate the non-equilibrium types of solidification, simulations with the Scheil conditions were performed on the Sr-containing alloys. AFM/SKPFM measurements were performed with a Park Systems XE-100 atomic force microscope in ambient conditions. Rectangular conductive cantilevers, ANSCM-PT from AppNano, were used to perform the measurements. These cantilevers have a Pt/Ir coating, a resonant frequency of 50–70 kHz and a spring constant of 1–5 N m^{-1}. The scanned areas were 10 × 10 μm (for the Al_2SrSi_2 particles) and 40 × 40 μm (for the Fe-rich primary eutectic particles). Topography and corresponding potential maps were measured simultaneously by a dynamic mode with a single-pass methodology. The measured potential, contact potential difference (CPD) between the tip of the cantilever and the sample, is associated with the difference between the work function of the tip and the sample. Therefore, this measured signal is directly correlated to the Volta potential of the sample's surface.[14,15] Finally, to report the real relation between the Volta potential values of the sample surface, the measured potential is inverted. A minimum of ten Fe-rich primary eutectic particles and ten Al_2SrSi_2 particles, all at different locations, were covered in different Volta potential maps in the Sr-containing alloy with 0.4 wt% Sr.

Results and Discussion

Microstructure characterisation.— *Thermo-Calc calculations.*— Thermo-Calc calculations were performed on the base alloy with addition of Sr to determine which phases are being formed during solidification and at which temperatures. These calculations reported the formation of five different phases starting from the liquid phase, these being: the aluminium matrix; the Al(Mn,Fe) phase, typically Al_6(Mn, Fe); the α-Al(Mn,Fe)Si phase, typically $\alpha - Al_{15}(Mn, Fe)_3Si_2$; the Al_3Zr phase and the Al_2SrSi_2 phase.[13] However, these calculations consider the case where solidification occurs at perfect thermodynamic equilibrium. Figure 1 shows the predicted mole fraction of all these phases as a function of the temperature. This Fig. 1c shows the well-known eutectoid transformation of the eutectic Al(Mn,Fe) phase to the α-Al(Mn,Fe)Si phase, occurring at about 646 °C. For the base alloy it is well known from literature that there are only four different phases formed during solidification from the liquid phase, namely: the aluminium matrix; the Al(Mn,Fe) phase, typically Al_6(Mn, Fe); the α-Al(Mn,Fe)Si phase, typically $\alpha - Al_{15}(Mn, Fe)_3Si_2$ and the Al_3Zr phase.[13] It seems that in the Sr-containing alloy all of the Sr will precipitate in the newly formed Al_2SrSi_2 phase with no Sr in the matrix, as can be seen in Table II.

In industrial processes, however, there will be no thermodynamic equilibrium during solidification of the melt. In order to simulate these non-equilibrium types of solidification new simulations with the Scheil conditions were performed on the Sr-containing alloy. Figure 2 reports, the mole fraction of all the formed phases as a function of temperature. The simulations with the Scheil conditions report the formation of six phases, namely: the aluminium matrix; the Al(Mn,Fe) phase, typically Al_6(Mn, Fe); the α-Al(Mn,Fe)Si phase, typically $\alpha - Al_{15}(Mn, Fe)_3Si_2$; the Al_3Zr phase; the β-AlFeSi phase, typically $\beta - Al_5FeSi$ and the Al_2SrSi_2 phase. These non-equilibrium simulations report the same five phases as were seen in the calculations considering equilibrium solidification. In addition the non-equilibrium simulations report an extra phase, the β-AlFeSi phase. The β phase might nonetheless not be found in the lab casted material, given the high Mn content in the alloy and the well-known fact that Mn stimulates the transformation of the β phase to the α phase.[16]

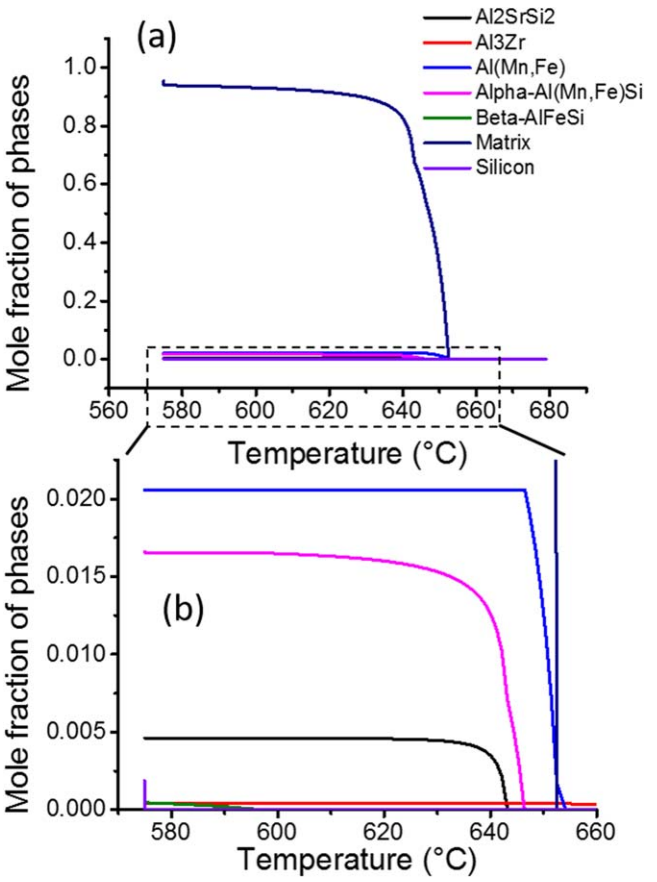

Figure 2. Thermo-calc simulation with the Scheil conditions of the solidification process of the base alloy with addition of Sr, (b) a magnified view of (a).

ToF-SIMS analysis.—ToF-SIMS analysis was performed on the 0.4 wt% Sr-containing alloy, Fig. 3a shows the area that was analysed. Figure 3b shows ToF-SIMS images of the Sr-containing alloy material. The Sr^+ ToF-SIMS image shows no Sr presence in the matrix, as it forms a separate phase as was predicted by the Thermo-Calc calculations. The overlays of the Mn^+ with the Sr^+ ToF-SIMS images and the Fe^+ with the Sr^+ ToF-SIMS images show that the Sr-phase is not coinciding with the Fe and Mn bearing phases. Furthermore, the Al + (saturated), the $AlOH^+$ and the Si^+ ToF-SIMS images report their presence in the matrix as well as in the other phases, like the Sr-bearing phase. To conclude, the ToF-SIMS analysis suggests the formation of the Al_2SrSi_2 phase in the Sr-containing alloy, as was predicted by the Thermo-calc calculations.

SEM/EDS analysis.—Figure 4a shows an SEM image of the microstructure of the base alloy. This figure reports the presence of the two eutectic primary phases, namely: the Al(Mn,Fe) phase, typically Al_6(Mn, Fe); the α-Al(Mn,Fe)Si phase, typically

Table II. Composition of the aluminium matrix (Mole percent) in the Sr-containing alloy, determined by thermo-calc.

Al	Si	Fe	Mn	Zr	Sr
100	7.43×10^{-7}	1.00×10^{-10}	4.92×10^{-8}	1.83×10^{-8}	1.00×10^{-10}

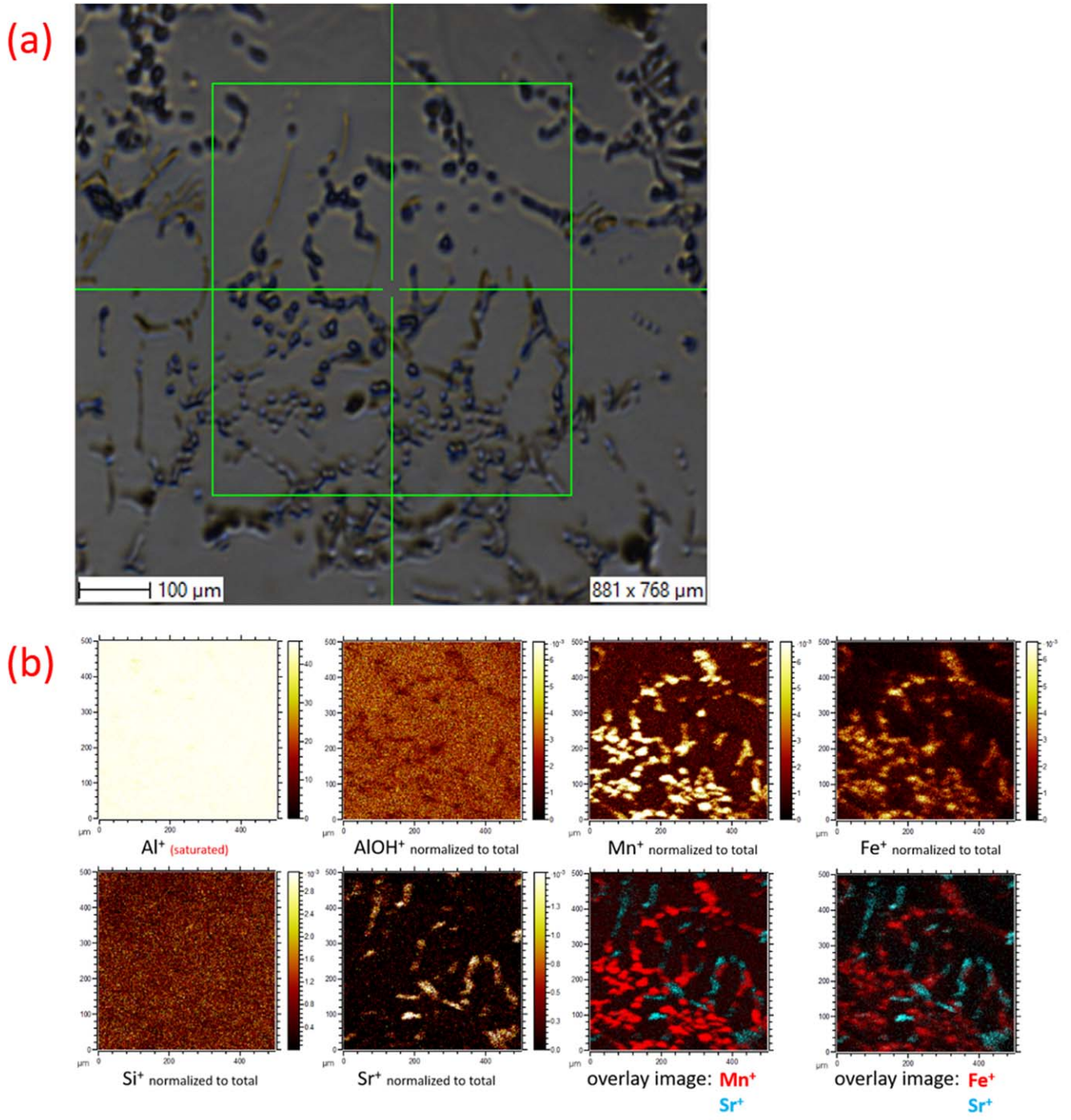

Figure 3. Optical view of the ToF-SIMS analysis area of the Sr-containing alloy material, the green grid denotes the area that is analysed (a) and ToF-SIMS images of the Sr-containing alloy material (b).

$\alpha - Al_{15}(Mn, Fe)_3Si_2$. These primary particles are rich in Fe, as can be seen in Table III. Furthermore, no β -AlFeSi phase was detected. Figure 4b shows a SEM image of the microstructure of the Sr-containing alloy, it reports the presence of the two eutectic primary phases. Additionally, no β-AlFeSi phase was detected and the primary phases were not visibly more refined compared to the base alloy. Moreover, it shows the presence of another phase, this being the Al_2SrSi_2 phase, as was already suggested by the Thermo-Calc calculations, the ToF-SIMS analysis and confirmed by Table III. This Al_2SrSi_2 phase has a needle like morphology, as can be seen in Fig. 4b with the Al_2SrSi_2 phase denoted by red arrows.

Macrohardness.—The macrohardness was determined for the base alloy as well as the Sr-containing alloys; these results can be seen in Table IV. Table IV reports a slight increase of macrohardness with the addition of Sr This increase in macrohardness with increasing Sr content could be explained by the increasing amount of the Al_2SrSi_2 particles, causing a hardening effect.

Electrochemical characterisation.— *Corrosion behaviour.*—The corrosion behaviour of the base alloy and the Sr-bearing alloys was studied by first determining the open circuit potential, followed by polarisation in the anodic and cathodic direction, in a 0.1 M NaCl electrolyte solution. Figure 5 shows the value of the OCP as a

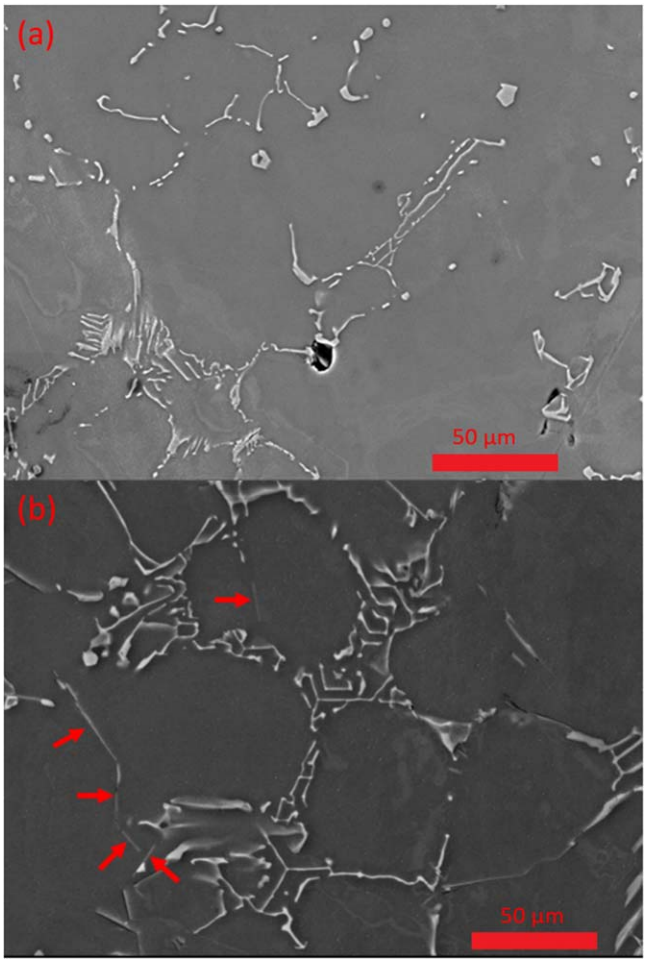

Figure 4. SEM images of the microstructure of the base alloy (a) and of the Sr-containing alloy, with the red arrows denoting the Al_2SrSi_2 phase (b).

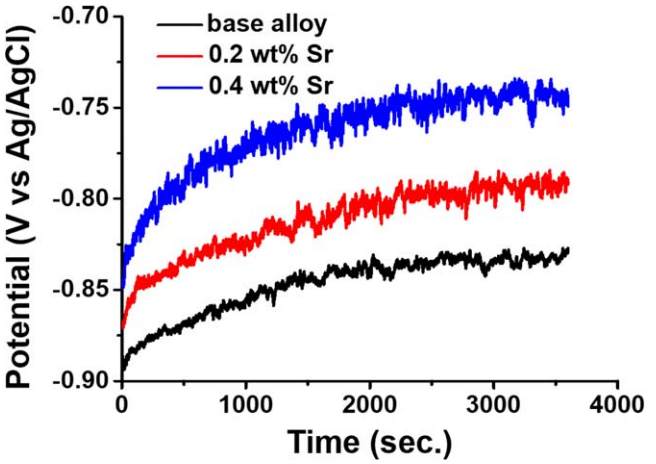

Figure 5. Open Circuit Potential (OCP) determination of the base alloy, the Sr-containing alloy with 0.2 wt% Sr and the Sr-containing alloy with 0.4 wt % Sr

Potentiodynamic polarization measurements were performed on all of the different alloys in aerated solution. The anodic polarization measurements showed an active behaviour for all samples and the anodic current density does not change significantly with the addition of Sr, as shown in Fig. 6a. In aerated solution, the pitting potential coincides with the corrosion potential. At this potential value, the lowest current density is measured. By increasing the applied potential a rapid increase in current density (as a result of the pitting process) can be clearly noticed. The pitting potential is shown to slightly increase with addition of Sr, as can be seen in Fig. 6a. On average, the pitting potential of the base alloy is -0.82 ± 0.01 V (vs Ag/AgCl), the Sr-containing alloy with 0.2 wt% Sr is -0.79 ± 0.02 V (vs Ag/AgCl) and the Sr-containing alloy with 0.4 wt% Sr is -0.75 ± 0.02 V (vs Ag/AgCl). This would suggest that the pitting resistance increases with the addition of Sr However, the cathodic polarisation measurements show the same cathodic limiting current density for all of the samples, as shown in Fig. 6b. This means that

Table III. Chemical composition (wt%) of a primary particle and a Sr-containing particle in the Sr-containing alloy with 0.4 wt% Sr, obtained by SEM/EDS.

	Si	Fe	Mn	Zn	Sr	Al
Primary particle	4.9 ± 0.8	6.3 ± 2.1	10.1 ± 2.9	1.1 ± 0.2	0	77.6 ± 4.6
Sr-containing particle	15.9 ± 0.8	0	0.2 ± 0.2	0.8 ± 0.1	21.5 ± 1.4	61.6 ± 1.9

Table IV. Macrohardness of the base alloy and the Sr-containing alloys.

Macrohardness (HRF)	Base alloy	Base alloy with 0.2 wt% Sr	Base alloy with 0.4 wt% Sr
Average	73.1 ± 1.5	76.7 ± 3.5	79.8 ± 1.4

function of time for all the alloys. This figure shows that the OCP value starts low but then increases as a function of time until it stabilises. The reason for this initial slight increase in the OCP values with time is not well understood, since several different parameters influence this value. Figure 5 further shows for all alloys a metastable behaviour, in the form of potential fluctuations. The initiation of the pitting process starts with the anodic dissolution of aluminium and a drop in the potential. After this anodic dissolution, the cathodic reactions, like oxygen reduction reactions, rapidly unfold at the surface resulting in a repassivation of the formed pit.[17,18] Moreover, Fig. 5 reports that the OCP increases with Sr content.

there is no change in the cathodic activity by addition of Sr to the base alloy. Therefore, the corrosion process, which is limited by the oxygen reduction reaction, is the same in all samples analysed. Generally, the cathodic activity is associated with the cathodic phases in the metal surface, which in the case of aluminium alloys these are generally the intermetallic particles, where most of the cathodic reactions take place. Furthermore, since the microstructural analysis revealed that for the Sr-containing alloys there is an extra phase present, namely the Al_2SrSi_2 phase, this could mean that the Al_2SrSi_2 phase in the Sr-containing alloys will not be contributing to the corrosion process.

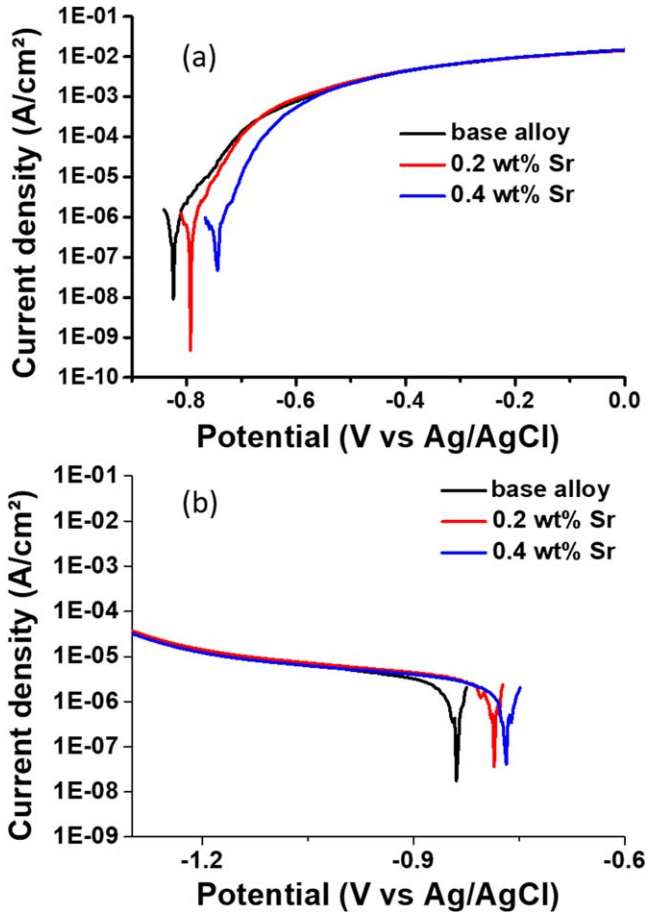

Figure 6. Anodic (a) and cathodic (b) potentiodynamic polarization measurements, in 0.1 M NaCl, of the Sr-containing alloy with 0.2 wt% Sr and the Sr-containing alloy with 0.4 wt% Sr

Corrosion morphology.—All the samples were immersed in a 0.1 M NaCl solution for 1 and 5 d in order to study the effect of Sr addition on the corrosion morphology. The base alloy shows pitting corrosion and trenching around the primary eutectic particles after 1 d immersion, originating from the micro galvanic coupling between these particles and the aluminium matrix, as seen in Fig. 7a.[19–21] The Sr-containing alloys show pitting corrosion and trenching around the primary eutectic particles as well after 1 d immersion, to the same extent as the base alloy, as shown in Fig. 7b. Moreover, this figure shows that the Al_2SrSi_2 particles, marked by the red arrows, do not contribute to the corrosion process. The samples immersed for 5 d show the same trend, with around the Sr-particles still no visible corrosion, as seen in Fig. 8. The lack of corrosion process around the Sr-particles was already suggested by the cathodic polarisation plots. This suggests that the Al_2SrSi_2 particles will not contribute to the initiation of corrosion. In other words, the pitting behaviour is not altered by the presence of these Al_2SrSi_2 particles, even though the Sr-containing alloys show a higher pitting potential.

Oxide layer analysis.—Figure 9 shows the XPS spectra of the surfaces of the base alloy (a) and the Sr-modified alloy with 0.4 wt% (b). This figure reports no difference in the XPS survey spectra between the Sr-modified and base alloy. Moreover, Sr was not detected in the XPS spectra, most likely because of the low content in the alloys (maximum 0.4 wt%). An example of a high resolution Al2p XPS spectrum is shown in Fig. 9c. This spectrum shows that the Al2p metal peak has closely spaced spin–orbit components which manifest as an asymmetric peak rather than outright splitting, as such the metal and oxide contribution was determined and from this the oxide thickness was calculated. As can be seen in Fig. 9c.

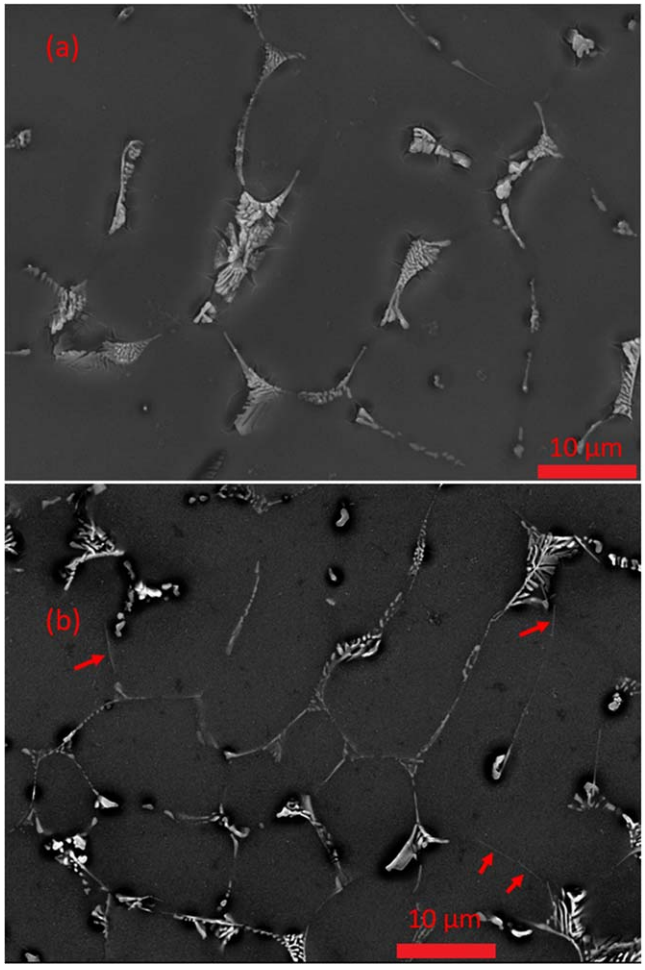

Figure 7. SEM images of immersed base alloy (a) and Sr-containing alloy (b) in 0.1 M NaCl solution for 1 d, with the red arrows marking the Al_2SrSi_2 particles.

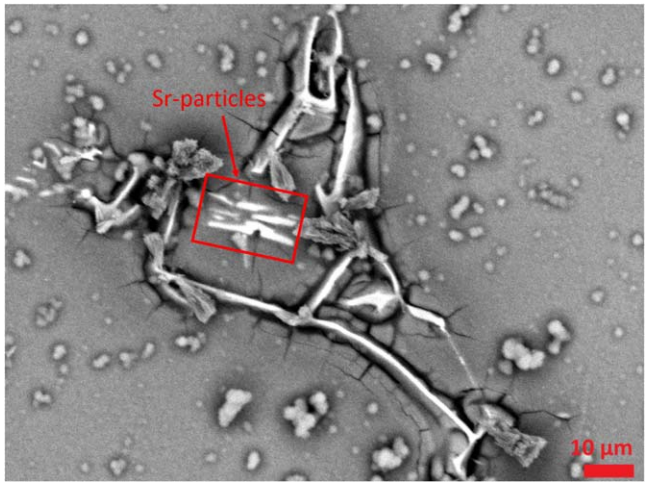

Figure 8. SEM images of immersed Sr-containing alloy in 0.1 M NaCl solution for 5 d, with the red rectangle marking the Al_2SrSi_2 particles.

The Strohmeier equation allows for the calculation of the oxide thickness from the XPS-obtained aluminium metal and oxide intensity peaks.[22,23] This method reported an oxide thickness of 3.8 nm for the base alloy and an oxide thickness of 3.7 nm for the Sr-containing alloy with 0.4 wt% Sr XPS analysis showed a comparable

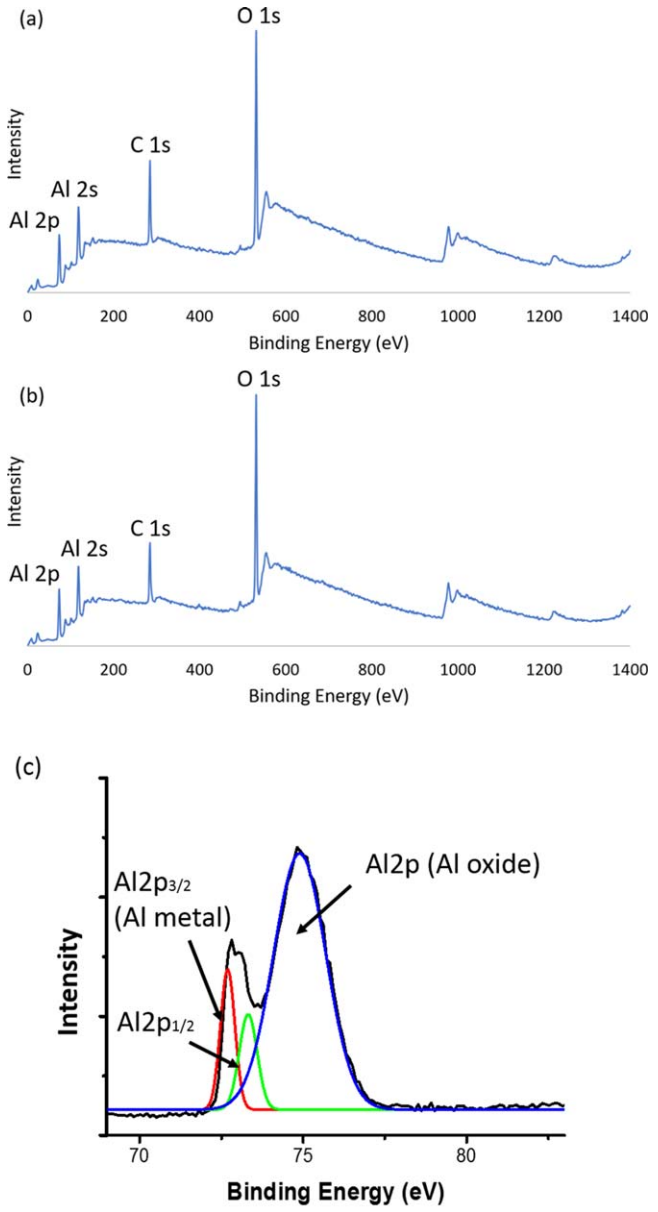

Figure 9. XPS survey of the base alloy (a) and the Sr-containing alloy with 0.4 wt% Sr (b). Example of the high resolution Al2p XPS spectrum obtained from the surface of the base alloy (c).

native oxide thickness for the base alloy and Sr containing alloy. However, to investigate whether there might be a local difference in oxide layer on top of the Al_2SrSi_2 particles and Fe-rich particles, Auger depth profiling was performed. The Auger depth profiles of the Sr-containing alloy with 0.4 wt% Sr on top of a Al_2SrSi_2 particle, a Fe-rich particle, and the matrix phase are seen respectively in Fig. 10. In these Auger depth profiles the native oxide thickness is given by the cross-over point between the aluminium and oxygen intensity lines, as marked by the red vertical lines in Fig. 10. The Auger depth profiles reveal the lowest native oxide thickness above the matrix phase and a slightly higher thickness above the Fe-rich particle. However, a significantly thicker oxide layer was observed on top of the Al_2SrSi_2 particle. The values of the oxide layer thickness are determined from the specific depth profiles of Fig. 10 for the different phases. The oxide layer on top of the matrix was calculated to be 2.4 nm, the oxide layer on top of the Fe-rich particle was calculated to be 4.0 nm, and the oxide layer on top of the Al_2SrSi_2 particle was calculated to be 6.4 nm. The Auger depth

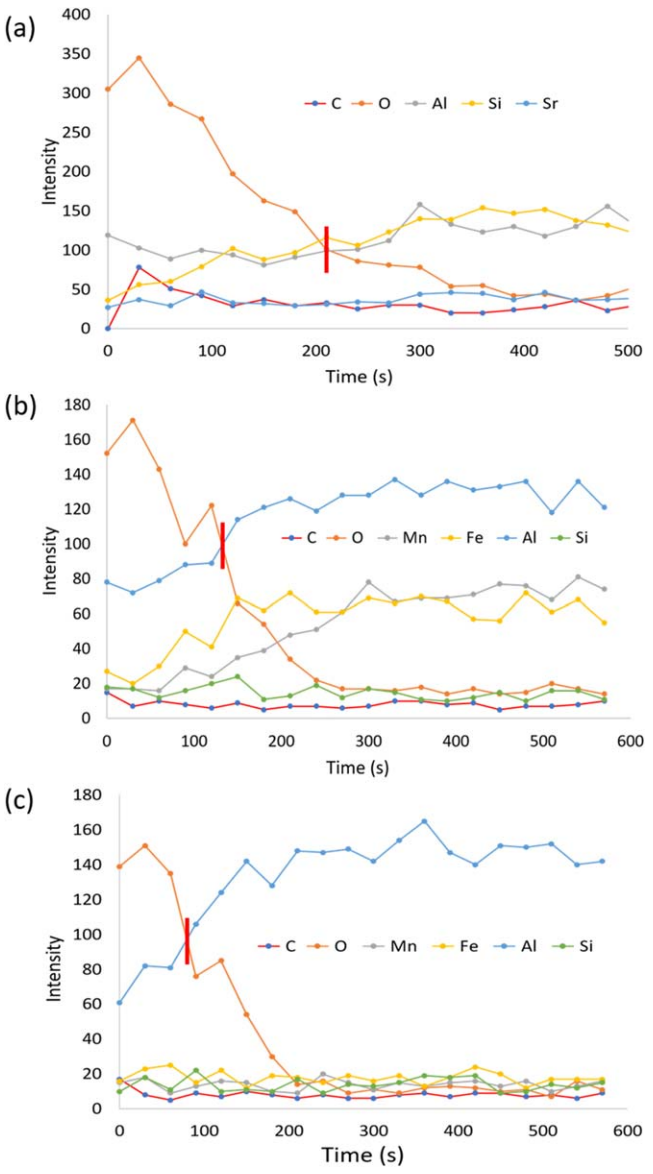

Figure 10. Auger depth profiles on top of: a Al_2SrSi_2 particle (a), a Fe-rich particle (b), and the matrix phase (c) in the Sr-containing alloy with 0.4 wt% Sr the red vertical lines denote the the cross-over point between the aluminium and oxygen intensity lines.

profiles thus clearly indicate a significantly thicker oxide layer on top of the Al_2SrSi_2 particle. This thicker oxide layer on top of the Al_2SrSi_2 particle could explain the reduced corrosion activity seen related to these particles.

The interaction between the intermetallic particles and the matrix.—Volta potential maps of a Sr-containing sample with 0.4 wt% Sr were made by use of SKPFM. Examples of these Volta potential maps are given in Fig. 11, EDS maps were performed to confirm the type of phases that were analysed. The Volta potential maps in Fig. 11 show that the intermetallic particles, these being the Fe-rich particles and the Al_2SrSi_2 particles, have a higher nobility compared to the aluminium matrix. This would suggest a cathodic behaviour of these intermetallic particles compared to the matrix. In the case of the Fe-rich intermetallic particles it was already shown by Davoodi et al. that they have a cathodic behaviour.[11–13] This cathodic behaviour results in micro galvanic coupling between these particles and the aluminium matrix, resulting in pitting corrosion of the matrix around them.

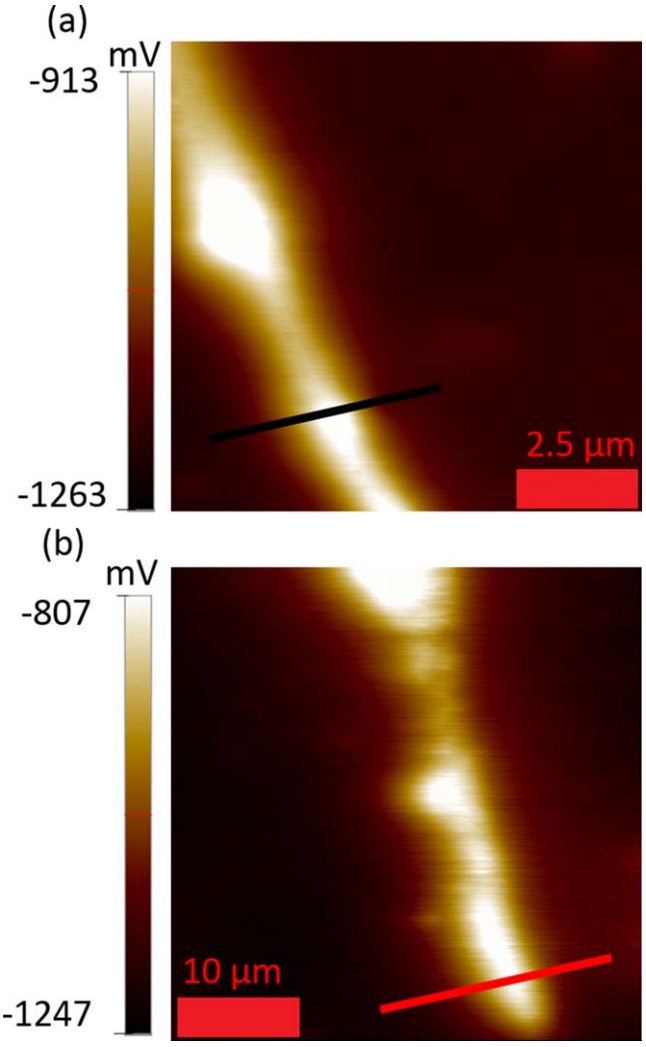

Figure 11. Volta potential maps covering a Al_2SrSi_2 particle (a) and an Fe-rich primary particle (b) in the Sr-containing alloy with 0.4 wt% Sr, the black and red line mark the positions of the scans.

However, in case of the Al_2SrSi_2 particles, which are also showing a higher Volta potential than the matrix, the SEM images did not show these particles to be electrochemically active, nor did the cathodic polarisation measurements reveal different activity of the Sr-containing alloy compared to the base alloy. On the other hand, their presence with higher nobility compared to the base alloy without these particles, could explain the slight shift to higher values of the OCP of the Sr-containing alloy compared to the base alloy.

However, it is not known why these Al_2SrSi_2 particles are not causing localised micro galvanic coupling like the Fe-containing phases with the matrix. A statistical analysis of the Volta potential difference between the intermetallic particles (the Fe-rich primary particles and the Al_2SrSi_2 particles) and the aluminium matrix was carried out: the average Volta potential value of the intermetallics was determined from the histogram of all Volta potentials measured on these intermetallic particles, while the average Volta potential of the matrix was obtained from the histograms of the Volta potential maps covering intermetallics and the matrix. The Volta potential difference between the Fe-rich primary particles and the matrix is on average about 295 ± 100 mV. The Volta potential difference between the Al_2SrSi_2 particles and the matrix is on average about 178 ± 120 mV, almost half compared to the Fe-rich primary particles. The Volta potential differences between the intermetallic particles and the matrix is also shown in the line scans (Fig. 12) performed on the Volta potential maps of Fig. 11. There is a

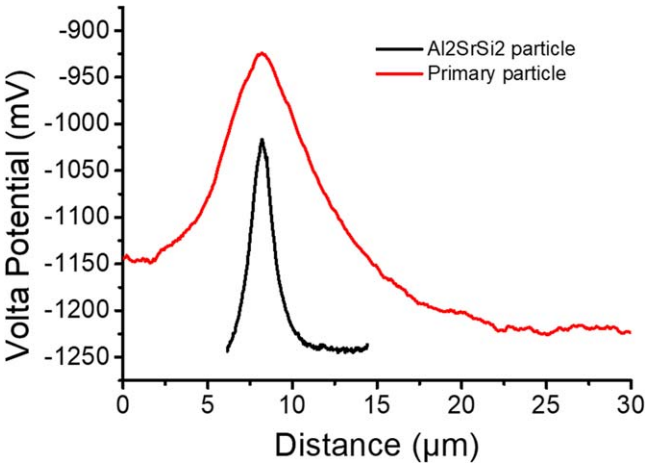

Figure 12. Line scans of the Volta potential maps covering two intermetallic particles (the Fe-rich primary particle and the Al_2SrSi_2 particle) and the surrounding aluminium matrix.

significantly lower Volta potential difference between the Al_2SrSi_2 particles and the matrix suggesting possibly a lower driving force for local galvanic coupling than for the Fe-containing phases. But, although it is lower, it is still more than high enough to cause galvanic coupling. Important to note however is that the Auger depth profiles showed a significantly thicker oxide layer on top of the Al_2SrSi_2 particles, which can have two important effects. Firstly, it has been shown in previous studies, that the thickness of the native oxide layer can have a great effect on the potential values measured by SKPFM.[24–26] Therefore, the considerably higher oxide thickness on top of the Sr-containing particles could be the cause of the relatively large value of Volta-potential measured on these particles. Secondly, it is most likely that this thicker oxide will contribute to the lack of corrosion activity seen near these particles. Additionally, it is not excluded that the Al_2SrSi_2 particles will only start contributing to the corrosion process in a later stage, once the corrosion activity and galvanic coupling between the Fe-rich primary particles and the matrix has diminished.

Furthermore, the Fe-rich particles are hard and high melting point particles; this combined with the larger difference in the coefficient of thermal expansion between Fe and Al compared Sr and Al, could result in the formation of a significantly larger amount of dislocations near the Fe-rich particles during solidification.[27] The higher dislocation density near the Fe-rich particles can be detrimental to the corrosion resistance, since near dislocations the anodic metal dissolution rate is increased by a local change of the electrochemical potential.[28–30] This may also contribute the higher activity of the aluminium matrix around the Fe-containing particles, compared to the matrix around the Sr-containing phases.

In general, the addition of Sr was shown to improve the hardness, without deteriorating the (local) corrosion properties of the alloy. This improvement was obtained by the formation of a new Sr-rich phase, namely the Al_2SrSi_2 phase. This Al_2SrSi_2 phase did not influence the corrosion resistance, even though higher pitting potentials were observed. The Sr-containing particles did not contribute to the corrosion process within the five day lasting NaCl solution immersion test, despite their cathodic behaviour compared to the Al matrix as measured by SKPFM. This demonstrates that the Sr-containing particles do not contribute to the corrosion initiation process.

Conclusions

This work studied the effect of Sr addition to the modified AA3003 on the microstructural and corrosion properties of this alloy. The following conclusions can be drawn:

- The thermodynamic calculations predicted the formation of a Sr-phase, namely the Al_2SrSi_2 phase, which was confirmed in the microstructural characterisation of the lab casted material.
- The Fe-rich primary phases were not visibly refined in the Sr-containing alloys compared to the base alloy.
- The Sr-containing alloys showed a higher microhardness, most likely due to the presence of the Al_2SrSi_2 phases.
- The Al_2SrSi_2 phase was shown to have a significantly thicker native oxide layer than the matrix and Fe-rich primary phases.
- The SKPFM measurements revealed that the Al_2SrSi_2 particles induce a significantly lower galvanic coupling with the matrix compared to the Fe-rich particles.
- The Al_2SrSi_2 particles do not appear to be electrochemically active during cathodic polarisation experiments and in immersion tests, even though a cathodic behaviour was measured by SKPFM measurements.
- Within the given conditions of the corrosion study (duration of immersion and electrolyte concentration) the Al_2SrSi_2 particles did not contribute to the corrosion process, due to the thicker oxide layer on top of the particles. This demonstrates that the Sr-containing particles do not contribute to the corrosion initiation process in this material studied.
- The Al_2SrSi_2 phase was reported not to deteriorate the corrosion properties, even though the Sr-containing alloys showed higher pitting potentials.

To conclude, the addition of Sr to the modified AA3003 is reported to improve the mechanical properties of the alloy, while not negatively affecting the corrosion resistance, by the formation of the Al_2SrSi_2 phase, that will not contribute to the corrosion and corrosion initiation process.

ORCID

Donovan Verkens https://orcid.org/0000-0003-2208-0892
Herman Terryn https://orcid.org/0000-0003-2639-5496

References

1. M. Timpel, N. Wanderka, R. Schlesiger, T. Yamamoto, N. Lazarev, D. Isheim, G. Schmitz, S. Matsumura, and J. Banhart, *Acta Mater.*, **60**, 3920 (2012).
2. G. Sigworth, *International Journal of Metal casting*, **2**, 19 (2008).
3. S. Farahany, A Ourdjini, and H. R Bakhsheshi-Rad, *Trans. Nonferrous Met. Soc. China*, **26**, 28 (2016).
4. H. Liao, G. Dong, and G. Sun, *J. Mater. Sci.*, **42**, 5175 (2007).
5. B. Zhu, M. Fedel, N. Andersson, P. Leisner, F. Deflorian, and C. Zanella, "The annual congress of the European Federation of Corrosion." *20th International Corrosion Congress and Process Safety Congress*, p 27 (2017).
6. P. Ashtari, H. Tezuka, and T. Sato, *Mater. Trans.*, **44**, 2611 (2003).
7. R. K. Gupta, R. Zhang, C. H. J. Davies, and N. Birbilis, *Corrosion*, **70**, 402 (2014).
8. P. Zhang, W. Xia, H. Yan, J. Chen, B. Su, X. Li, and X. Li, *Materials and Corrosion*, **70**, 1798 (2019).
9. F. N. Afshar, A. M. Glenn, J. H. W. De Wit, H. Terryn, and J. M. C. Mol, *Electrochim. Acta*, **104**, 48 (2013).
10. S. Y. Paredes-Dugarte and B. Hidalgo-Prada, *Procedia Mater. Sci.*, **8**, 82 (2015).
11. A. Davoodi, J. Pan, C. Leygraf, and S. Norgren, *J. Electrochem. Soc.*, **155**, C138 (2008).
12. A. Davoodi, J. Pan, C. Leygraf, and S. Norgren, *Electrochim. Acta*, **52**, 7697 (2007).
13. A. Davoodi, J. Pan, C. Leygraf, and S. Norgren, *J. Electrochem. Soc.*, **155**, C211 (2008).
14. J. H. W. De Wit, *Electrochim. Acta*, **49**, 2841 (2004).
15. P. Schmutz and G. S. Frankel, *J. Electrochem. Soc.*, **145**, 2285 (1998).
16. R. Rana, R. Purohit, and S. Das, *International Journal of Scientific and Research Publications*, **2**, 1 (2012).
17. J. A. Richardson and G. C. Wood, *Corros. Sci.*, **10**, 313 (1970).
18. S. I. Pyun and W. J. Lee, *Corros. Sci.*, **43**, 353 (2001).
19. R. G. Buchheit, *J. Electrochem. Soc.*, **142**, 3994 (1995).
20. N. Birbilis and R. G. Buchheit, *J. Electrochem. Soc.*, **152**, B140 (2005).
21. S. Paredes-Dugarte, B. Hidalgo-Prada, R. Avila-Godoy, and M. Briceno- Valero, *Rev. Tec. La Fac. Ing. Univ. Del Zulia*, **30**, 168 (2007).
22. T. A. Carlson and G. E. McGuire, *J. Electron Spectrosc. Relat. Phenom.*, **1**, 161 (1972).
23. B. R. Strohmeier, *Surf. Interface Anal.*, **15**, 51 (1990).
24. R. I. Revilla, H. Terryn, and I. D. Graeve, *Electrochem. Commun.*, **93**, 162 (2018).
25. T. H. Muster and A. E. Hughes, *J. Electrochem. Soc.*, **153**, B474 (2006).
26. K. A. Yasakau, A. N. Salak, M. L. Zheludkevich, and M. G. S. Ferreira, *J. Phys. Chem. C*, **114**, 8474 (2010).
27. Y. S. Touloukian, *Thermophysical Properties of Matter* 12(Thermal Expansion, IFI/Plenum, New York) (1975).
28. G. B. Hamua, D. Eliezer, and L. Wagner, *J. Alloys Compd.*, **468**, 222 (2009).
29. K. D. Ralston and N. Birbilis, *Corrosion*, **66**, 1 (2010).
30. C. Liu, R. I. Revilla, D. Zhang, Z. Liu, A. Lutz, F. Zhang, T. Zhao, H. Ma, X. Li, and H. Terryn, *Corros. Sci.*, **138**, 96 (2018).